ACS APPLIED MATERIALS & INTERFACES

Research Article

Cite This: ACS Appl. Mater. Interfaces XXXX, XXX, XXX–XXX

www.acsami.org

Longitudinal Monitoring of Biofilm Formation via Robust Surface-Enhanced Raman Scattering Quantification of *Pseudomonas aeruginosa*-Produced Metabolites

Cuong Quoc Nguyen,[†] William John Thrift,[†] Arunima Bhattacharjee,[†] Saba Ranjbar,[†] Tara Gallagher,[‡] Mahsa Darvishzadeh-Varcheie,[§] Robert Noboru Sanderson,[∥] Filippo Capolino,[§] Katrine Whiteson,[‡] Pierre Baldi,[⊥] Allon I. Hochbaum,[†] and Regina Ragan*[,†]

[†]Department of Chemical Engineering and Materials Science, [‡]Department of Molecular Biology and Biochemistry, [§]Department of Electrical Engineering and Computer Science, [∥]Department of Physics and Astronomy, and [⊥]Department of Computer Science, University of California, Irvine, Irvine, California 92697, United States

Supporting Information

ABSTRACT: Detection of bacterial metabolites at low concentrations in fluids with complex background allows for applications ranging from detecting biomarkers of respiratory infections to identifying contaminated medical instruments. Surface-enhanced Raman scattering (SERS) spectroscopy, when utilizing plasmonic nanogaps, has the relatively unique capacity to reach trace molecular detection limits in a label-free format, yet large-area device fabrication incorporating nanogaps with this level of performance has proven difficult. Here, we demonstrate the advantages of using chemical assembly to fabricate SERS surfaces with controlled nanometer gap spacings between plasmonic nanospheres. Control of nanogap spacings via the length of the chemical crosslinker provides uniform SERS signals, exhibiting detection of pyocyanin, a secondary metabolite of *Pseudomonas aeruginosa*, in aqueous media at concentration of 100 pg·mL^{-1}. When using machine learning algorithms to analyze the SERS data of the conditioned medium from a bacterial culture, having a more complex background, we achieve 1 ng·mL^{-1} limit of detection of pyocyanin and robust quantification of concentration spanning 5 orders of magnitude. Nanogaps are also incorporated in an in-line microfluidic device, enabling longitudinal monitoring of *P. aeruginosa* biofilm formation via rapid pyocyanin detection in a medium effluent as early as 3 h after inoculation and quantification in under 9 h. Surface-attached bacteria exposed to a bactericidal antibiotic were differentially less susceptible after 10 h of growth, indicating that these devices may be useful for early intervention of bacterial infections.

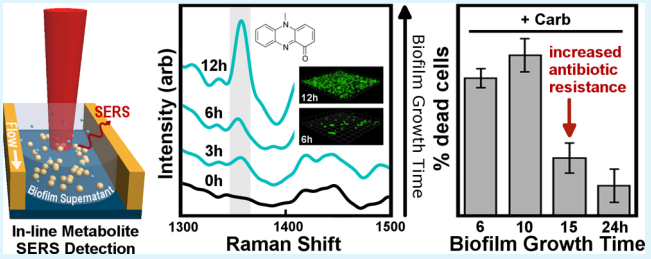

KEYWORDS: *self-assembly, surface-enhanced Raman scattering, statistical spectral analysis, biofilms, metabolomics, quorum sensing, biosensor*

INTRODUCTION

During biofilm formation, differential gene expression is regulated through a cell density-dependent mechanism called quorum sensing (QS).[1,2] Soon after surface attachment, bacteria begin producing extracellular polymeric substances and QS signaling molecules.[3] Once formed, a combination of physical mechanisms and genetic and metabolic adaptations within the biofilms imparts extreme antibiotic tolerance or resistance to the constituent cells,[4] which can withstand up to 1000 times higher doses of antibiotics than their free floating planktonic counterparts.[5] While new antimicrobial strategies are being developed to combat antibiotic resistance, here we investigate a promising parallel strategy, sensing bacterial metabolites associated with QS for early detection of *Pseudomonas aeruginosa* biofilm formation at a stage where antibiotic treatment has higher efficacy. *P. aeruginosa* is a biofilm-forming, opportunistic pathogen that is associated with the contamination of medical devices and respiratory infections in immunocompromised patients[6,7] and is one of the most common bacteria isolated in chronic wounds.[8] Among the many virulence factors and QS compounds that *P. aeruginosa* produces is pyocyanin,[9] a redox-active secondary metabolite which can act as a terminal signaling factor in the QS process.

Interestingly, recent Raman spectroscopy-based studies have demonstrated the ability to distinguish between species of bacteria,[10−12] identify molecules enriched in particular species, and even detect specific local metabolic activity in environmental samples using stable isotope probing techniques.[13] Raman spectroscopy has been demonstrated to outperform matrix-assisted laser desorption ionization−time of flight mass spectrometry in accurately discriminating between *Acinetobacter baumannii* strains.[12] Raman spectra provide "molecular finger-

Received: December 6, 2017
Accepted: March 28, 2018
Published: March 28, 2018

DOI: 10.1021/acsami.7b18592
ACS Appl. Mater. Interfaces XXXX, XXX, XXX–XXX

prints" composed of the vibrational spectrum of molecules serving as a label-free detection method. Biologically relevant concentrations of metabolites often range from nM to mM levels in clinical samples,[14,15] and the ability to detect them has enormous potential for enabling personalized medicine. The limit of detection (LOD) and quantification range of metabolite concentration needed at physiologically significant levels in biological samples, though this may vary with molecules and environments,[16] is often in the μM range,[17] and thus requires large and reproducible enhancements of Raman signals. Surface-enhanced Raman scattering (SERS), when employing plasmonic nanogaps, is capable of providing necessary enhancements to achieve detection at biologically relevant concentrations. SERS has been used to distinguish between colony biofilms of bacteria species during maturation phases[18] and even detect pyocyanin in spiked saliva down to 2.1 μg·mL^{-1} (10 μM)[19] and spiked in subcutaneous implants in mice down to 0.1 μM.[20] Yet challenges still exist in incorporating nanogaps with large and uniform enhancement factors in device architectures with nM detection limits and quantification spanning the range of metabolite concentrations found in biological samples.

SERS enhancement factors due to plasmonic nanogaps are highly dependent on the distance between plasmonic nanoantennas, increasing monotonically with decreasing gap size. Statistical analysis of various size-controlled nanogaps using DNA tethering observed single molecule SERS intensity when nanogaps are on the order of 0.5−0.9 nm.[21,22] At nanogap distances below approximately 0.5 nm, depolarization effects attributed to quantum tunneling reduce enhancements.[23] Reaching sub-nanometer nanogap dimensions over large area without large variations is difficult, and thus, SERS substrates often exhibit tradeoffs between reproducibility and large enhancement factors. Yet it is necessary to have both uniform and large enhancement factors across SERS substrates to reproducibly achieve low detection limits in quantitative sensing applications. Consider that at extremely low concentrations, analyte molecules will not be uniformly distributed across the surface.[24,25] SERS measurements on a mixture of two different analytes determined that single molecule sensing events occur at nM concentration as not every molecule in the scattering volume will reside in a hotspot.[25,26] Inherent variances in SERS substrates' enhancement factors only worsen any analyte's location-dependent signal variations and will lead to large SERS intensity fluctuations. While such surfaces may produce a low LOD because of the presence of a few hotspots on the surface, the limit of quantification (LOQ) will be much higher. Thus, increasing the uniformity and density of nanogaps with high enhancements will lead to a higher probability that an analyte will adsorb on a hotspot in the illuminating laser spot size and thereby reproducibly contribute to the SERS signal at low concentrations.

Here, large-scale uniformity in hotspot intensity from nanoantennas on SERS substrates is achieved using a hierarchical self-assembly method for fabricating Au nanospheres into close-packed structures, referred to as oligomers, on a diblock copolymer template. Assembly combines long range, electrohydrodynamic (EHD) flow,[27−30] and short range, chemical crosslinking, driving forces to provide a high density of oligomers with sub-nanometer nanogap spacing. Induced by an electric field in colloidal solution, EHD flow promotes lateral motion and close-packing of nanospheres in the colloid at the electrode surfaces, assembling transient close-packed oligomers. Transient oligomers are frozen using 1-ethyl-3-(3-(dimethylamino)propyl)carbodiimide (EDC), a carbodiimide crosslinker, to form an anhydride bridge between the carboxylic acid ligands on Au nanospheres. We have previously reported that this process achieves a high yield of close-packed oligomers composed of 10 nanospheres or less with gap spacing of 0.9 nm, having an electric field enhancement on the order of 600 in the hotspot region.[31] Close-packing is also advantageous as it allows for variability of oligomer orientation with respect to polarization of incident light. In a close-packed oligomer, the plasmon resonance will most closely reflect that of a linear oligomer along the polarization axis.[31,32]

When using benzenethiol as the analyte, here we report that SERS signals exhibit a relative standard deviation (RSD) of 10% across a 100 μm × 100 μm area with over 1000 different measurements. This achievable uniform SERS response allows for the incorporation in microfluidic device architectures and spectral data analysis using multivariate machine learning algorithms.[33−35] A large number of training data sets and the full spectra collected from SERS substrates are necessary for accurate quantitative analysis by accounting for signal variance inherent to SERS. By combining uniform SERS substrates having high signal enhancements with multivariate statistical analysis of SERS spectra, we are able to differentiate pyocyanin in the complex soup of biological media at concentrations down to 1 ng·mL^{-1} (4.8 nM) and robustly quantify concentrations spanning 5 orders of magnitude. Moreover, rapid SERS analysis in solutions negates the need to grow biofilms directly on SERS substrates[20] or to drop-cast plasmonic clusters on static biofilms,[18] thus allowing instantaneous quantification of pyocyanin for the detection of biofilm formation on any surface. Longitudinal monitoring of the supernatant from bacterial cultures in microfluidic devices exhibits SERS signal from pyocyanin as early as 3 h after *P. aeruginosa* culture inoculation. This is before surface-attached bacteria exhibits a decreased susceptibility to bactericidal antibiotic carbenicillin that was measured at 10 h. Low-cost fabrication of nanoantennas with nanometer-scale nanogaps over large areas enabled by self-assembly and statistical spectral analysis of SERS data demonstrate the capacity for fabricating device architectures capable of early detection of biofilms enabling effective antimicrobial treatment.

RESULTS AND DISCUSSION

Large-Area Uniformity of SERS Substrates. Directing the assembly of Au oligomers with uniformly distributed electromagnetic hotspots over large areas is achieved by utilizing EHD flow to drive chemical crosslinking to form nanogaps with sub-nanometer gap spacing as reported previously.[31] The chemical assembly is facilitated using a two-step growth process: (1) electrophoretic sedimentation driving chemical crosslinking of Au nanoparticle seeds onto a working electrode and (2) growing oligomers via EHD flow and stabilizing via chemical crosslinking. During electrophoresis, depicted in Figure 1a, lipoic acid-functionalized Au nanoparticle monomer seeds are chemically assembled on amine-functionalized poly(methyl methacrylate) (PMMA) regions of a diblock copolymer poly(styrene-*b*-methyl methacrylate) (PS-*b*-PMMA)-coated working electrode using 1-ethyl-3-(3-(dimethylamino) propyl)carbodiimide/*N*-hydroxysulfosuccinimide (EDC/s-NHS) carbodiimide chemistry (inset). In the second deposition step, an applied field deforms the ionic double layer around the Au seeds, shown on the right of Figure 1a, inducing

DOI: 10.1021/acsami.7b18592
ACS Appl. Mater. Interfaces XXXX, XXX, XXX−XXX

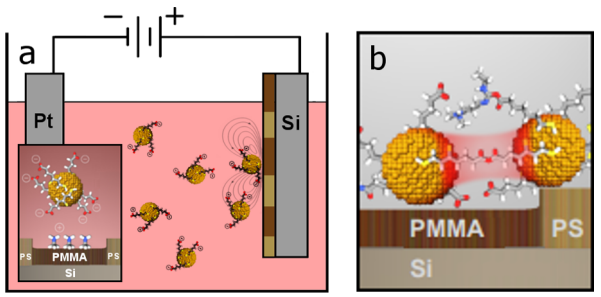

Figure 1. Schematic overview of chemical assembly of SERS substrates. (a) Lipoic acid-functionalized Au nanoparticles are electrophoretically driven toward a working electrode. Au seeds chemically crosslink with amine-functionalized PMMA regions on self-organized diblock copolymer PS-*b*-PMMA template (inset). The resultant EHD flow field around the seed entrains the nearby nanoparticles forming transient oligomers. (b) Illustration of the anhydride bridge that forms between carboxylic acid and acylisourea on neighboring nanoparticles that stabilizes oligomers when the external field is turned off.

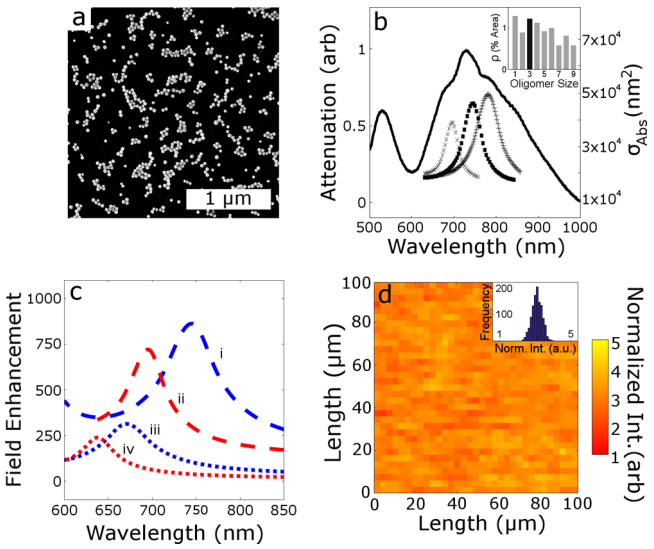

Figure 2. (a) SEM micrograph of self-assembled Au oligomers. (b) Attenuation curve of SERS substrates in DI water. Dotted curves represent absorption cross section of a dimer (×), linear trimer (squares), and linear quadrumer (+) from full-wave simulations. Inset shows oligomers distributions in percent area on SERS substrate calculated from SEM images acquired over 10 μm^2. (c) Calculated field enhancement of Au (i) linear trimer with 0.9 nm gap, (ii) dimer with 0.9 nm gap, (iii) linear trimer with 2 nm gap, and (iv) dimer with 2 nm gap from full-wave simulations. Curves (i) and (ii) are offset by 100 for clarity. (d) Normalized SERS intensity map of benzenethiol's 1573 cm^{-1} vibrational band. Inset shows distribution of normalized intensity with a RSD of 10.4%.

an osmotic flow toward the seeds' equator, termed the EHD flow.[30,36,37] These flow fields entrain the nearby nanospheres and drives them toward Au seeds to form transient close-packed oligomers, which are subsequently stabilized through an acylisourea−carboxylic acid reaction that forms anhydride bridges between nanospheres, shown in Figure 1b. These bridges result in oligomers with uniform interparticle gap spacings of approximately 0.9 nm, corresponding to the sulfur−sulfur distance of an anhydride bridge calculated from atomistic simulations and observed in transmission electron microscopy.[31]

A scanning electron microscopy (SEM) image of a SERS substrate composed of self-assembled oligomers is displayed in Figure 2a. The size distribution in percent area (Figure 2b inset), determined from image analysis of SEM images using Wolfram Mathematica, indicates that trimers are observed with the highest probability, with quadrumers being the second. The absorption cross section of a dimer, linear trimer, and linear quadrumer with a nanogap size of 0.9 nm—corresponding to the calculated sulfur−sulfur distance of an anhydride bridge—was calculated from full-wave simulations and shows good agreement with the fine structure observed in the UV−visible measurement as shown in Figure 2b. This agreement suggests that the measured attenuation is dominated by frequencies near the trimer resonance with contributions from frequencies associated with dimers and quadrumers that are blue- and red-shifted, respectively. Larger oligomers observed in the SEM image of Figure 2a contribute to the broad shoulder at higher wavelength. This observation can be understood by considering the effect of the close-packed arrangement of nanospheres in oligomers on their plasmon resonance. It has been previously shown using dark field microscopy and full-wave simulations that an oligomer's plasmon mode is only slightly perturbed by the addition of a nanosphere when the added nanosphere is unaligned with the incident beam's polarization. For example, a hexamer made up of two trimers on top of each other has a plasmon mode that is slightly red-shifted from that of a linear trimer.[32] Consider that for a close-packed oligomer to have more than 4 nanospheres in a row, it must be composed of more than 21 nanospheres. From the oligomer size distribution, Figure 2b inset, it was determined that, by number, 98% (88% by area) of the oligomers are composed of 21 nanospheres or less. It is then unsurprising that the resonance is dominated by dimers, trimers, and quadrumers. Full-wave simulations of the electric field enhancement—$|E_{olig}|/|E_0|$, where E_{olig} and E_0 are the plane wave field with and without oligomers, respectively—was performed for nanogaps of 0.9 and 2 nm in dimers and linear trimers and are shown in Figure 2c. As expected, the resonance red-shifts as the gap distance decreases. Furthermore, increasing the gap spacing from 0.9 to 2 nm reduces the calculated field enhancement from 621 to 240 (762 to 314) in a dimer (linear trimer). The SERS enhancement can be estimated as the fourth power of the field enhancement, $|E_{olig}|/|E_0|^4$, and thus even slight variations in field enhancement will lead to large variations in SERS intensity. Overall, the plasmon resonance is less affected by close-packed oligomer size than the resultant field enhancement in the nanogaps when the spacing decreases below 2 nm. Thus, chemically controlled gap spacing enables uniform SERS intensity, as observed in Figure 2d.

Figure 2d displays the normalized SERS intensity of a benzenethiol vibration band, 1573 cm^{-1}, acquired over a 100 $\mu m \times 100$ μm area. The SERS intensity has a RSD of 10.4%. While nanogap spacing of 0.9 nm is important to achieve large and uniform SERS enhancements, at the same time, the assembly method provides a sufficiently broad band response, ranging over a window of 625−875 nm in the attenuation measurement, to enhance signals at both the plasmon excitation wavelength and Raman scattered wavelength. The uniform SERS response with large enhancements over large area enables the use of these SERS substrates in device architectures. Of further significance, it also enables the acquisition of large data sets needed for statistical analysis enabling quantitative detection.

DOI: 10.1021/acsami.7b18592
ACS Appl. Mater. Interfaces XXXX, XXX, XXX−XXX

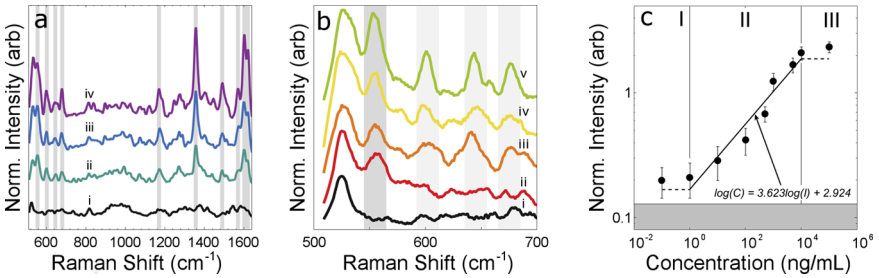

Figure 3. (a) SERRS spectra of (i) DI water, (ii) 1 μg·mL^{-1}, (iii) 10 μg·mL^{-1}, and (iv) 100 μg·mL^{-1} pyocyanin in water. Gray bars indicate Raman bands of pyocyanin. (b) SERRS spectra of (i) DI water, (ii) 100 pg·mL^{-1}, (iii) 1 ng·mL^{-1}, (iv) 10 ng·mL^{-1}, and (v) 100 ng·mL^{-1} pyocyanin in water. Dark gray bar highlights pyocyanin's 552 cm^{-1} band, whereas light gray bars indicate other pyocyanin Raman bands. (c) Dose−response relationship of pyocyanin and normalized SERS intensity at 552 cm^{-1}. Error bars depict standard deviation calculated from 100 measurements.

Quantification and Detection of Pyocyanin in Aqueous Media. Pyocyanin exhibits a broad absorption band from 550 to 900 nm;[20,38] thus using a 785 nm laser to excite nanoantennas results in surface-enhanced resonance Raman scattering (SERRS). SERRS spectra of aqueous pyocyanin from 1 μg·mL^{-1} (4.8 μM) to 100 μg·mL^{-1} (480 μM) (Figure 3a) displays clear Raman bands similar to pyocyanin spectra reported using surfaces with Ag colloids[19] and Ag and Au nanorods[20,39] at 552, 1353, 1602, and 1620 cm^{-1}. These bands rise at a concentration as low as of 100 pg·mL^{-1} (480 pM), as exemplified in Figure 3b for the band 552 cm^{-1}. The log−log dose−response curve of pyocyanin at 552 cm^{-1} (Figure 3c) reveals a linear regime between 1 ng·mL^{-1} and 10 μg·mL^{-1}, consistent with Langmuir adsorption kinetics; similar linear relationships with concentration are also observed for other pyocyanin vibrational bands, and results are shown in Figure S1. Within this linear regime, pyocyanin concentration can be quantified using the formula shown in eq 1 with R^2 = 0.951.

$$\log C = a \log I + b \tag{1}$$

Here a and b are fitting constants with value of 3.623 and 2.924, respectively, while C and I represent pyocyanin concentration and normalized SERRS intensity at 552 cm^{-1}, respectively. For concentrations below the LOQ, 1 ng·mL^{-1}, SERS substrates detection of pyocyanin was determined by comparing the signal and background at 552 cm^{-1} per guideline EP17 of the Clinical and Laboratory Standards Institute.[40] The limit of blank (LOB) is calculated by adding the mean background signal [deionized (DI) water] $\overline{I}_{bg}$ at 552 cm^{-1} to 1.645 its standard deviation σ_{bg}, as shown in eq 2

$$\mathrm{LOB} = \overline{I}_{bg} + 1.645\sigma_{bg} \tag{2}$$

Detection is defined in the standard manner where the mean signal, $\overline{I}_D$, at 552 cm^{-1} is at least 1.645 standard deviations, σ_D, larger than or equal to the LOB, as shown in eq 3

$$\overline{I}_D - 1.645\sigma_D \geq \mathrm{LOB} \tag{3}$$

From this analysis, SERS substrates exhibit detection of pyocyanin in aqueous media at a concentration of 100 pg·mL^{-1}, above which one can observe pyocyanin signals above the background in Figure 3c. We did not measure pyocyanin at lower concentrations because our interest was in establishing a LOD in biological media. These results are discussed in the following section.

Training Data Acquisition and Building Multivariate Predictive Model. Using linear regression on a single Raman band allows for facile comparison with other SERS surfaces in the literature as it is widely used for quantitative calibration.[19,20,39,41−46] While this method is sufficient for the analysis of a pure analyte in water, it discards the remaining rich spectral information in each spectrum and can lose sensitivity when other molecules are present in solution as is the case when monitoring biofilm growth. Alternatively multivariate analysis, specifically partial least square (PLS) regression, analyzes the full spectra collected from SERS substrates and improves LOQs in complex media.[47] Thus, we capitalize on the uniform SERS response of our surfaces to acquire necessary training data and employ PLS analysis to quantify pyocyanin in a more complex biological media, an important requirement for diagnostic applications. Training data sets, composed of SERRS spectra from known concentrations of pyocyanin spiked in LB media, generate a robust PLS-predictive model for pyocyanin concentration in the increased background noise of the biological media. The multivariate model predictive capability is subsequently demonstrated by quantifying pyocyanin production from *P. aeruginosa* planktonic cultures during in vitro growth.

First, we demonstrate the suitability of our substrates for detecting pyocyanin in complex media by comparing SERRS spectra of blank LB media, LB media spiked with 10 μg·mL^{-1} of pyocyanin alongside spectra of cell-free supernatants collected from mid-stationary phase cultures of wild-type *P. aeruginosa* PA14 and its phenazine-deficient mutant strain Δphz1/2 as a control (Figure 4a). The Δphz1/2 strain does not produce phenazines; hence its SERRS spectrum (multiplied a factor of 5 for clarity) indeed lacks the vibrational fingerprint of pyocyanin; it is similar to the spectrum obtained for blank LB media. Meanwhile, SERRS spectra of wild-type PA14 and pyocyanin in LB broth exhibit similar features, including distinct pyocyanin vibrational bands and thus confirming the suitability of our substrates for the task. While pyocyanin signals are clearly seen here, signal interference from other molecules is amplified at low concentration, requiring more sophisticated analysis.

The calibration data sets that were acquired by collecting SERRS spectra of LB media spiked with 100 pg·mL^{-1} to 100 μg·mL^{-1} pyocyanin generated a predictive model of pyocyanin concentration in LB media using PLS regression. From the 400 spectra collected for each pyocyanin dose, 380 were randomly selected as training set and the remaining 20 withheld as the testing set. To optimize the model, over- and under-fitting are avoided by using 10 PLS components where a minimum in root mean square error of cross validation (RMSECV) is observed, displayed in inset of Figure 4b. With the testing set, the model demonstrates accurate prediction between 1 ng·

DOI: 10.1021/acsami.7b18592
ACS Appl. Mater. Interfaces XXXX, XXX, XXX−XXX

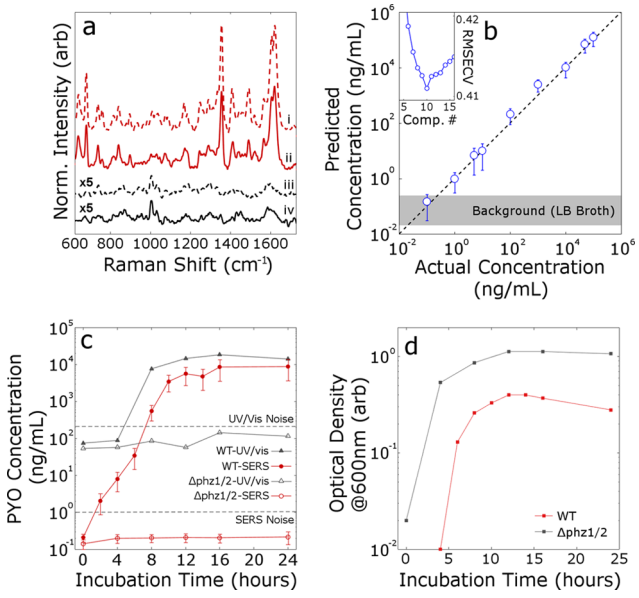

Figure 4. (a) SERRS fingerprint of (i) bacteria-free supernatant from mid-stationary phase cultures of wild-type *P. aeruginosa* PA14, (ii) 10 $\mu g \cdot mL^{-1}$ pyocyanin in LB broth, (iii) phenzine-null mutant strain Δphz1/2, and (iv) LB broth. (b) Pyocyanin concentration predicted by the PLS model for spectra in the testing set. Error bars depict standard deviation calculated from 20 measurements. Inset shows RMSECV of the PLS model with respect to the number of components used. (c) Pyocyanin concentration in bacteria-free supernatants of wild-type *P. aeruginosa* PA14 and its phenazine-null strain over 24 h. Concentrations from SERS and UV−vis measurements are calculated using the trained PLS model and reported molar absorptivity $\varepsilon = 4.31 \times 10^3$ mol^{-1} cm^{-1} at $\lambda_{max} = 690$ nm (from ref 48), respectively. Error bars show standard deviation calculated from 400 measurements. (d) Growth curves for planktonic cultures of *P. aeruginosa* PA14 and its phenazine-null mutant strain as determined from optical density.

mL^{-1} and 100 $\mu g \cdot mL^{-1}$, as shown in Figure 4b. Fitting the predicted versus actual concentration with a line having a slope of 1—representing perfect predictive capability—gives a R^2 value of 0.956.

Pyocyanin Quantitative Detection in Complex Media. The generated predictive model was used to quantify pyocyanin from SERRS spectra of cell-free conditioned growth medium of wild-type *P. aeruginosa* and Δphz1/2 as a function of incubation time. For each incubation time point, 400 SERRS spectra were collected within the span of less than 4 min, and their corresponding pyocyanin concentrations were calculated using the PLS model; the average concentration for incubation times ranging from 0 to 24 h is shown in Figure 4c. The performance of SERRS-PLS was compared with UV−vis absorption spectroscopy typically employed to quantify pyocyanin. Pyocyanin concentrations were calculated from UV−vis absorption peaks using the reported molar absorptivity $\varepsilon = 4.31 \times 10^3$ mol^{-1} cm^{-1} at $\lambda_{max} = 690$ nm.[48]

The pyocyanin-deficient Δphz1/2 strain was used to calculate the instrument noise and contributions from the background media. This yielded the UV−vis LOD as 197 ng·mL^{-1} (0.94 μM), equivalent to three standard deviations above the background of the Δphz1/2 strain. This value agrees well with the reported LOD of 1 μM for UV−vis.[49] The UV−vis data is also plotted in Figure 4c for comparison with SERRS data. The LOD of SERRS observed in Figure 4b is 1 ng·mL^{-1} (4.8 nM) using the same definition for differentiating from background noise and PLS model discussed above. Thus, SERS substrates are able to detect pyocyanin as early as 2 h of shaking culture growth and quantify the concentration as 2.5 ng·mL^{-1} (12 nM), as opposed to after 8 h of shaking culture growth when using UV−vis absorption. From 8 h onward, quantitative performance of the two methods is comparable. The sharp increase in pyocyanin concentration detected by SERRS from 2 to 8 h correlates with the exponential growth phase of *P. aeruginosa* in the shaking culture, which is observed in Figure 4d as an increase in optical density and thereby accumulation of biomass. Overall, these data validate the robustness of SERS substrates toward the detection of pyocyanin in complex media.

Monitoring Biofilm Formation via Pyocyanin Quantification. Here, we integrate microfluidic channels with SERS substrates to perform in-line sampling of biofilm's effluent, thus enabling rapid quantitative detection of pyocyanin as a means to longitudinally monitor biofilm growth. *P. aeruginosa* biofilms were grown in tryptone broth (TB) medium as previously described.[50] Effluent from the biofilm growth channel is delivered to a microfluidic channel with Au oligomers assembled on the surface as illustrated in Figure 5a. Every 3 hours, 200 SERRS spectra are collected in the effluent with a total acquisition time of 2 min, thus eliminating the need for performing chloroform extraction and incubating,[20] or evaporating the solvent on SERS surfaces.[39] To quantify pyocyanin, a suitable predictive model was generated by repeating PLS analysis on the training dataset acquired using the appropriate collection parameters for TB media (as opposed to LB in planktonic cultures growth) as reported in our methods. The resulting LOD from this analysis is 10 ng·mL^{-1}. Using the model, pyocyanin was detected in the SERRS signal above the LOD starting between 6 and 9 h after inoculating as observed in Figure 5b. Thus, the time of quantification (TOQ) falls within this range. Pyocyanin concentration after 9 h was determined to be 24 ng·mL^{-1} (115 nM), above the determined LOD. The half-life of pyocyanin desorption from the surface was determined to be on the order of 11 min from subsequent SERS measurements from samples immersed in water, exposed to 1 $\mu g \cdot mL^{-1}$ (4.8 μM) pyocyanin, rinsed, and reimmersed in water, as shown in Figure S2 of Supporting Information. Thus, the calculated concentrations are indicative of the instantaneous production of pyocyanin in the biofilm growth channel. Investigation of results generated from the model shows that some spectra at 3 and 6 h reveals Raman bands associated with pyocyanin above the background. By analyzing the individual spectra, it was determined that 7.8 and 14.3% of the spectra at 3 and 6 h, respectively, show a pyocyanin concentration above the background; representative spectra are plotted in Figure 5c. This fraction increases to 70.3, 96.7, and 100% for the subsequent time points. This is consistent with nonuniform distribution of pyocyanin on the substrate surface at low concentrations. Hence, while the averaged concentration of pyocyanin calculated for the set of Raman spectra at 3 and 6 h of the biofilm growth lies below the LOD, a fraction of those spectra shows that pyocyanin is detected at those early time points. Thus, 3 h is set as the time of detection (TOD). The calculated concentrations of pyocyanin correlate with the time-dependent accumulation of biofilm biomass obtained from the analysis of fluorescence images of the microfluidic growth channels (Figure 5d). Representative confocal fluorescence images of the growth channels show the initial stages of

DOI: 10.1021/acsami.7b18592
ACS Appl. Mater. Interfaces XXXX, XXX, XXX−XXX

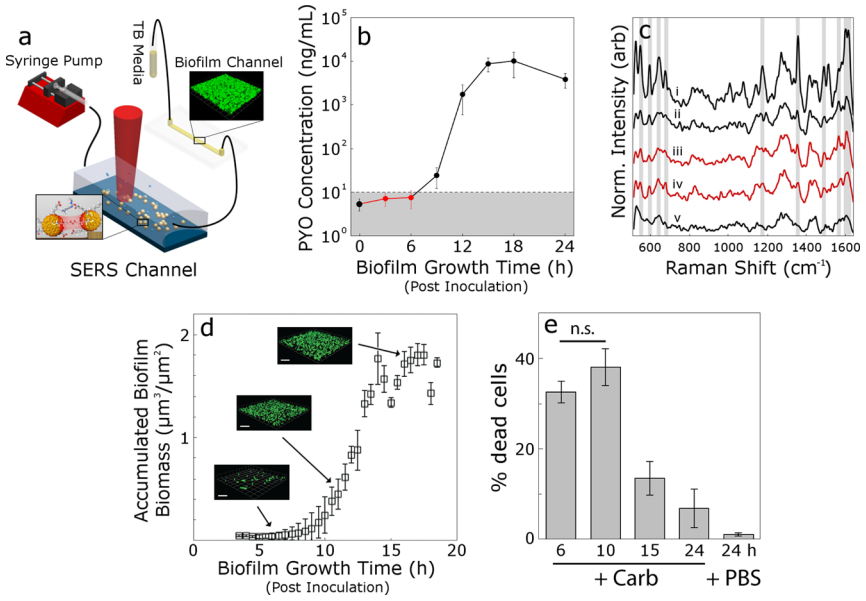

Figure 5. (a) Schematic of the biofilm in-line measurements setup. (b) Pyocyanin concentration predicted by the PLS model from SERS spectra of various time. Each data point represents the averaged of predicted concentrations, and error bars show standard deviation calculated from 200 measurements. (c) Individual representative SERS spectra at (i) 12 (ii) 9, (iii) 6, and (iv) 3 h contrasted with a spectrum of (v) TB media. Gray bars indicate pyocyanin vibrational bands. (d) Accumulated biomass of biofilm growth in the flow cell over time. Error bars depict standard deviations calculated from n = 3 independent growth channels. Confocal fluorescence microscopy images show representative bacterial accumulation on the glass surface at the time points indicated by the arrows (scale bars are 20 μm). (e) Susceptibility of surface-attached bacteria to carbenicillin treatment at the specified growth times. Error bars depict standard deviation of dead cell fraction calculated from n = 3 biological replicates.

bacterial cell adhesion (6 h), microcolony formation (10 h), and three-dimensional growth of biofilms above the channel surface (16 h). The biomass and imaging data indicates that the biofilm formation can be monitored reliably after TOQ. More significantly, it reveals that the earliest detection of biofilms, corresponding to TOD, occurs during the initial stages of bacterial cell adhesion, earlier than that observed in fluorescence confocal images.

Bacterial biofilms impart antibiotic resistance and tolerance on constituent cells via several distinct mechanism.[4] These mechanisms are characteristic of bacterial phenotypes and properties of mature biofilms; hence, early treatment with antibiotics can be more effective than equivalent treatment of mature biofilms. The potential for early detection to provide a therapeutic improvement for infection outcomes was assessed by measuring the antibiotic susceptibility of surface-attached bacteria at different stages of biofilm growth. Bacteria exposed to a bactericidal antibiotic, carbenicillin, were differentially susceptible after 10 h of growth, after which their susceptibility decreased significantly with increasing growth time as they transition into a more antibiotic-tolerant state (Figure 5e); this transition is also captured as the sharp increase in pyocyanin concentration measured from SERRS in Figure 5b between 9 and 12 h. A control biofilm was grown for 24 h and exposed to phosphate-buffered saline (PBS) instead of carbenicillin indicates no statistically significant difference between the antibiotic susceptibility of cells grown in flow channels for 6 and 10 h. Consequently, the detection of a *P. aeruginosa* infection and intervention at early stages of colonization (<10 h growth) show the potential to substantially improve the effectiveness of antibiotic treatment.

CONCLUSION

Chemically assembled SERS substrates, using EHD flow to initiate chemical crosslinking, yield uniform nanogap spacings of 0.9 nm that proves advantageous for quantitative molecular detection. Full-wave simulations of near-field enhancements comparing 1 and 2 nm nanogaps show that variation of this parameter is critical to achieve high and reproducible SERS intensity needed to generate reliable training sets for machine learning algorithms. Large area signal uniformity, low excitation power, 14.6 μW, and short integration time, 0.1 s, allow for integration of SERS substrates in a device platform and the rapid acquisition of large data sets for statistical analysis. SERRS substrates exhibit the ability to detect pyocyanin in aqueous media at concentration of 100 pg·mL^{-1} when individual pyocyanin Raman bands are investigated. In more complex media, PLS analysis of spectral data enables robust quantification of pyocyanin spanning 5 orders of magnitude in biologically relevant levels between 1 ng·mL^{-1} and 100 μg·mL^{-1}. Integration of microfluidic architectures with SERS substrates facilitates in-line sampling of the effluent medium for longitudinal monitoring of pyocyanin concentration during *P. aeruginosa* biofilm formation. Measured pyocyanin concentration in the effluent medium correlates with the accumulated biofilm biomass obtained from confocal fluorescence images. More significantly, pyocyanin can be detected as early as 3 h after inoculation. A sharp increase in pyocyanin concentration is observed between 9 and 12 h after inoculation; this corresponds to decreased susceptibility of surface-attached bacteria to bactericidal antibiotic carbenicillin at 10 h. Thus, detecting microbial production of metabolites associated with QS with chemically assembled SERS substrates and analysis using machine learning algorithms lay out a promising strategy for detection of metabolites in biological media that can be pursued in future studies for more complex systems.

DOI: 10.1021/acsami.7b18592
ACS Appl. Mater. Interfaces XXXX, XXX, XXX−XXX

EXPERIMENTAL METHODS

Materials. Random copolymer poly(styrene-*co*-methyl methacrylate)-*α*-hydroxyl-*ω*-tempo moiety (PS-*r*-PMMA) (M_n = 7.4 kg mol^{-1}, 59.6% PS) and diblock copolymer poly(styrene-*b*-methyl methacrylate) (PS-*b*-PMMA) (M_n = 170-b-144 kg mol^{-1}) were purchased from Polymer Source, Inc. (Dorval, Canada). Gold nanospheres with diameter of 40 nm and lipoic functionalization were purchased from Nanocomposix (San Diego, CA). Si(001) wafers with resistivity of 0.004 Ω cm were purchased from Virginia Semiconductor (Frederickburg, VA). Hydrofluoric acid (HF) was purchased from Fisher Scientific (Pittsburg, PA). 2-(*N*-Morpholino)ethanesulfonic acid (MES) 0.1 M buffer was purchased from Pierce (Rockford, IL). 1-Ethyl-3-[3-dimethylaminopropyl]carbodiimide hydrochloride, s-NHS, dimethyl sulfoxide (DMSO), ethylenediamine (ED), toluene, ethanol, isopropanol (IPA), potassium carbonate, and 52-mesh Pt gauze foil were purchased from Sigma-Aldrich (St. Louis, MO). Nanopure DI water at 18.2 MΩ cm^{-1} was obtained from Milli-Q Millipore System.

Self-Assembly of SERS Substrates. Si wafers were cleaned in 10% HF to remove the native oxide. *The potential of HF to cause severe injury mandates extreme caution during usage.* Random copolymer PS-*r*-PMMA and diblock copolymer PS-*b*-PMMA solution in toluene (1 wt %) were spun coat on the flat Si surface and annealed at 198 °C to form thin films as described in previous work.[51] PMMA regions are selectively functionalized with amine end-groups by first immersing in DMSO and then in ED/DMSO solution (5 v/v %) for 5 min each step and without rinsing in between. The substrate is then washed with IPA for 1 min and dried under nitrogen.

Lipoic acid-functionalized 40 nm Au nanospheres in aqueous solution is concentrated twofold by adjusting the pH to 8 with potassium carbonate and centrifuging for 25 min at 1700 rcf and redispersed in DI water. Concentrated Au nanosphere solution (3 mL) is added to a 10 mL beaker, followed by 35 μL of freshly prepared 20 mM s-NHS in 0.1 M MES buffer and 35 μL of freshly prepared 8 mM EDC in 0.1 M MES buffer. The solution is swirled and moved on a hotplate to be heated to 8 °C. A 1 cm × 1 cm Pt mesh and 1 cm × 1 cm Si substrate are stabilized using alligator clips and placed into the solution vertically as the anode and cathode, respectively. A DC regulated power supply was used to apply a voltage of 1.2 V for 10 min to drive electrophoretic sedimentation of Au nanospheres to the surface. EDC initiated carbodiimide cross-linking chemistry is used to covalently bind carboxylic acid-functionalized Au nanospheres to the selectively amine-functionalized PMMA regions of the template via an amide bond.[51] The substrate, Pt mesh, and beaker are rinsed with IPA for 1 min and dried under nitrogen. The process is repeated on the same substrate with a freshly concentrated Au nanosphere solution but with 30 μL of EDC and s-NHS solution. Here, EHD flow around previously attached nanospheres drives nanospheres to chemically crosslink via EDC coupling chemistry to nanospheres assembled in the first step. Finally, the diblock copolymer layer is etched under oxygen plasma (50 W, 60 s) in the PC2000 Plasma Cleaner from South Bay Technology (San Clemente, CA) to remove organic groups from nanoparticle surfaces. The assembly on indium tin oxide (ITO)-coated glass is carried out identically, with the exception of the surfaces undergoing oxygen plasma etching at 100 W for 1 min before spin coating PS-*r*-PMMA.

Characterization. Images of SERS substrates are collected with a Magellan XHR scanning electron microscope (FEI). UV−vis absorption measurements of SERS substrates are carried out using a Shimadzu UV-1700 absorption spectrometer. Absorption spectra are taken of ITO-coated glass substrates taped (away from the beam path) on to a quartz cuvette filled with DI water.

***P. aeruginosa* Cell-Free Supernatant Preparation.** Wild-type *P. aeruginosa* (strain PA14[52]) shaking culture supernatant was used to measure pyocyanin production over time. PA14 was streaked onto the lysogeny broth (LB, EMD Millipore) agar plates from frozen glycerol stocks and grown overnight at 37 °C. Shaking cultures were inoculated from single colonies on the LB plate into 5 mL of liquid LB and grown at 37 °C on an orbital shaker overnight. Shaking culture (50 μL) was diluted into 24 mL of 10 g·L^{-1} tryptone media (Bacto tryptone, BD Scientific), and this subculture was grown at 37 °C on an orbital shaker. Aliquots were taken periodically from the shaking subculture for optical density measurements. To measure pyocyanin production, *P. aeruginosa* conditioned medium was isolated by centrifuging the 2 mL cultures at 15 000*g* and passing the resulting supernatant through a 0.2 μm PES vacuum filter (Corning). The filtered supernatants were dropped onto the SERS substrates and measured within 1 h from their collection time.

Fluidic Device Fabrication and Biofilm Growth. The microfluidic device consists of two channels, one for the biofilm and the other for the SERS substrate. Microfluidic channels for the biofilm were made by bonding the plasma-activated surfaces of polydimethylsiloxane with a glass slide. The SERS substrate and a glass slide are separated by an adhesive spacer of 100 μm thickness (3M 415) with channel design laser cut (Epilog Fusion Laser Cutter) in the adhesive layer.

P. aeruginosa biofilms for in-line detection of pyocyanin were grown in the above microfluidic devices as previously described using a *P. aeruginosa* strain constitutively expressing yellow fluorescent protein (YFP).[50] *P. aeruginosa* cells were seeded with no flow in the biofilm growth channel for 2 h. The fluid feed was then switched to sterile tryptone media, and the outlet of the channel was connected to the SERS channel input. The 0 h SERRS measurements were collected once the in-line device is fully connected, prior to start of the flow. Media was then pulled through the in-line detection device at 10 μL·h^{-1}, and SERRS spectra were collected at the indicated time points. Identical biofilms were grown and imaged in the flow cells to measure the time-dependence of the biofilm growth. The biofilm volume was obtained from Volocity imaging analysis software (PerkinElmer) of confocal fluorescence images of the YFP-producing biofilms. SERRS collection parameters are described below.

Antibiotic Susceptibility Measurements. *P. aeruginosa* biofilms were grown for 10, 15, and 24 h on glass coverslips submerged in 2 mL of TB supplemented with 3 g·L^{-1} NaCl in sterile, six-well tissue culture plates (Fisher Scientific). After the indicated growth time, the growth media was aspirated and the biofilms on the coverslips were rinsed once with PBS while still in the wells. The PBS rinse solution was then aspirated and replaced with 600 μg·mL^{-1} carbenicillin (minimum inhibitory concentration in *P. aeruginosa* strain PA14 128 μg·mL^{-1})[53] in PBS or PBS only for the control. Biofilms were soaked in the antibiotic or control solutions for 3 h, rinsed again with PBS, and then stained with live/dead cell viability assay stains, propidium iodide and Syto 9 (Fisher Scientific) at 2 μM final concentration each, for 15 min. Coverslips were rinsed once more in PBS, removed from the wells and placed face down on a microscope slide for confocal fluorescence imaging. The fraction of dead cells was calculated using the biovolumes of each color channel (red and green) obtained from Volocity imaging analysis software (PerkinElmer) of confocal fluorescence images of biofilms.

At 6 h biofilm growth, the washing steps described above removed all cells from the coverslips. Instead, the antibiotic susceptibility of surface-attached bacteria was measured from cells grown in microfluidic devices. After 6 h of growth, as described above for pyocyanin detection experiments, the input line was changed from TB to 600 μg·mL^{-1} carbenicillin in PBS for 3 h. The input line was then changed again to BacLight for 15 min and finally PBS for 30 min, after which the cells attached to the channel surface were imaged and the dead cell fraction was quantified by counting the individual cells of each color channel.

Spectroscopic Measurements Instrumentation and Procedure. Surface enhanced Raman spectroscopy measurements are conducted using a Renishaw InVia Raman Microscope system. A 785 nm continuous wave laser is chosen to excite near the plasmon resonance of Au nanoparticle assemblies as determined from electromagnetic simulations and ultraviolet−visible absorption measurements.[31]

In droplet measurements, as referred to in the main text, a 60× water immersion objective with 1.2 NA is used for illumination and collection. Approximately, 150 μL of solution of interest is transferred onto SERS substrates, and the measurements are acquired with laser

DOI: 10.1021/acsami.7b18592
ACS Appl. Mater. Interfaces XXXX, XXX, XXX−XXX

power and acquisition time of 7.3 μW and 0.5 s, respectively, over area specified for each case. SERS substrates are cleaned with IPA and DI water for 1 min each and dried under nitrogen between measurements. One substrate was used per set of measurements (concentrations or time points).

For in-line measurements, a 50× objective is used. Measurements are taken with laser power and acquisition time of 14.6 μW and 0.1 s, respectively. Illumination and collection were done through the SERS microfluidic channel.

Spectra Processing and Analysis. Raman scattering spectra processing and analysis were performed off-line using MATLAB R2016b (The MathWorks Inc, Natrick, MA). Each spectrum undergoes baseline correction, smoothing with Savitzky−Golay, and normalization to the average intensity of Si second-order vibrational band, reported between 920 and 1045 cm^{-1},[54] from the substrate. This allows for comparison of different samples where slight intensity variations may arise because of the deviations in optical collection in the experimental setup. Specifically, the range of 920 and 970 cm^{-1} was used because of the appearance of pyocyanin ring stretching vibrational band at 975 cm^{-1}. When preparing SERRS spectra for full-spectrum PLSs regression, a constant k = 1.0067 was added to the processed signals to eliminate negative values in the calibration matrix associated with variations due to noise. This is necessary as signals are then log-transformed before analysis with PLS regression. PLS regression combines characteristics of principal component analysis with multiple linear regression to predict a set of dependent variables from a large set of independent variables.[55]

Simulations. Full-wave simulations (frequency domain finite elements method solver) are implemented in CST Microwave Studio (CST AG). We calculate the absorption cross sections of several nanosphere oligomers: dimers, linear trimers, and linear quadrumers. The structure is as follows. Au nanospheres of 40 nm in diameter with 0.9 nm interparticle gaps[31] are partially embedded in a 40 nm PMMA layer[56] with their centers 8 nm above the PMMA. The PMMA layer is directly above a 150 nm ITO layer, which is directly above a 2 μm glass layer. The upper medium surrounding nanospheres is water. The total size of the structure in x−y plane (transverse plane) is assumed to be 4 μm × 4 μm, which is approximately 4 times larger than the largest excitation wavelength of 900 nm, and we applied software's open boundary condition. Au permittivity was calculated from the Drude model with parameters extracted from Grady.[57] The relative electric permittivity used for water, PMMA, glass, and ITO are 1.77, 2.47, 2.3207, and adapted from Moerland,[58] respectively. The permittivity in the gap region was unknown due to anhydride bonding[31] and thus was approximated by performing a parameter sweep of the gap permittivity and calculating the absorption of the dimer configuration to determine which best corresponds with the observed dimer peak at 686 nm. The resulting permittivity of 2.25 was used in simulations. Oligomers are excited with plane wave illumination at normal incidence with electric field polarization along the axis of the linear oligomers, and the absorption cross section of the structures is determined.

Field enhancement was also calculated from full-wave simulations of dimers and linear trimers with 0.9 and 2 nm interparticle gaps using the same conditions. Field enhancement is defined in eq 4.

$$\mathrm{FE} = |E_{olig}|/|E_0| \tag{4}$$

$|E_{olig}|$ represents the electric field magnitude at the center of the gap in the oligomer (dimer or trimer), and $|E_0|$ is the electric field magnitude at the same location in the absence of the structure.

■ ASSOCIATED CONTENT

Supporting Information

The Supporting Information is available free of charge on the ACS Publications website at DOI: 10.1021/acsami.7b18592.

Dose−response relationships of SERRS intensity for additional commonly observed pyocyanin vibrational modes at 1620, 1602, and 1353 cm^{-1}; details on the estimation of pyocyanin desorption half-life from SERRS intensity at 1620, 1602, 1353, and 552 cm^{-1} before, during, and after exposure to 1 $\mu g \cdot mL^{-1}$ (4.8 μM) pyocyanin (PDF)

■ AUTHOR INFORMATION

Corresponding Author

*E-mail: rragan@uci.edu.

ORCID

Pierre Baldi: 0000-0001-8752-4664

Allon I. Hochbaum: 0000-0002-5377-8065

Regina Ragan: 0000-0002-8694-5683

Notes

The authors declare no competing financial interest.

■ ACKNOWLEDGMENTS

The authors acknowledge the National Science Foundation EECS-1449397 for funding this work. The authors would like to thank Computer Simulation Technology (CST) of America, Inc. for providing CST Microwave Studio. W.J.T. acknowledges support from the National Science Foundation BEST IGERT Program (NSF DGE-1144901). A.B. acknowledges fellowship support from the Schlumberger Foundation. A.I.H. and S.R. acknowledge research support from AFOSR grant FA9550-17-1-0913. The authors also acknowledge the use of the facilities within the Laser Spectroscopy Facility, the Laboratory for Fluorescence Dynamics, and the Laboratory for Electron and X-ray Instrumentation (LEXI) center at the University of California, Irvine.

■ REFERENCES

(1) De Kievit, T. R.; Gillis, R.; Marx, S.; Brown, C.; Iglewski, B. H. Quorum-Sensing Genes in Pseudomonas Aeruginosa Biofilms: Their Role and Expression Patterns. *Appl. Environ. Microbiol.* **2001**, *67*, 1865−1873.

(2) Miller, M. B.; Bassler, B. L. Quorum Sensing in Bacteria. *Annu. Rev. Microbiol.* **2001**, *55*, 165−199.

(3) Kolter, R.; Greenberg, E. P. Microbial Sciences: The Superficial Life of Microbes. *Nature* **2006**, *441*, 300−302.

(4) Anderson, G. G.; O'Toole, G. A. Innate and Induced Resistance Mechanisms of Bacterial Biofilms. *Bacterial Biofilms; Current Topics in Microbiology and Immunology*; Springer: Berlin, Heidelberg, 2008; pp 85−105.

(5) Malone, M.; Goeres, D. M.; Gosbell, I.; Vickery, K.; Jensen, S.; Stoodley, P. Approaches to Biofilm-Associated Infections: The Need for Standardized and Relevant Biofilm Methods for Clinical Applications. *Expert Rev. Anti-Infect. Ther.* **2017**, *15*, 147−156.

(6) Hunter, R. C.; Klepac-Ceraj, V.; Lorenzi, M. M.; Grotzinger, H.; Martin, T. R.; Newman, D. K. Phenazine Content in the Cystic Fibrosis Respiratory Tract Negatively Correlates with Lung Function and Microbial Complexity. *Am. J. Respir. Cell Mol. Biol.* **2012**, *47*, 738−745.

(7) Whiteson, K. L.; Meinardi, S.; Lim, Y. W.; Schmieder, R.; Maughan, H.; Quinn, R.; Blake, D. R.; Conrad, D.; Rohwer, F. Breath Gas Metabolites and Bacterial Metagenomes from Cystic Fibrosis Airways Indicate Active PH Neutral 2,3-Butanedione Fermentation. *ISME J.* **2014**, *8*, 1247−1258.

(8) Serra, R.; Grande, R.; Butrico, L.; Rossi, A.; Settimio, U. F.; Caroleo, B.; Amato, B.; Gallelli, L.; de Franciscis, S. Chronic Wound Infections: The Role of Pseudomonas Aeruginosa and Staphylococcus Aureus. *Expert Rev. Anti-Infect. Ther.* **2015**, *13*, 605−613.

(9) Davies, J. C. Pseudomonas Aeruginosa in Cystic Fibrosis: Pathogenesis and Persistence. *Paediatr. Respir. Rev.* **2002**, *3*, 128−134.

(10) Lorenz, B.; Wichmann, C.; Stöckel, S.; Rösch, P.; Popp, J. Cultivation-Free Raman Spectroscopic Investigations of Bacteria. *Trends Microbiol.* **2017**, *25*, 413−424.

DOI: 10.1021/acsami.7b18592
ACS Appl. Mater. Interfaces XXXX, XXX, XXX−XXX

(11) Wu, X.; Huang, Y.-W.; Park, B.; Tripp, R. A.; Zhao, Y. Differentiation and Classification of Bacteria Using Vancomycin Functionalized Silver Nanorods Array Based Surface-Enhanced Raman Spectroscopy and Chemometric Analysis. *Talanta* **2015**, *139*, 96−103.
(12) Ghebremedhin, M.; Heitkamp, R.; Yesupriya, S.; Clay, B.; Crane, N. J. Accurate and Rapid Differentiation of Acinetobacter Baumannii Strains by Raman Spectroscopy: A Comparative Study. *J. Clin. Microbiol.* **2017**, *55*, 2480−2490.
(13) Berry, D.; Mader, E.; Lee, T. K.; Woebken, D.; Wang, Y.; Zhu, D.; Palatinszky, M.; Schintlmeister, A.; Schmid, M. C.; Hanson, B. T.; et al. Tracking Heavy Water (D2O) Incorporation for Identifying and Sorting Active Microbial Cells. *Proc. Natl. Acad. Sci. U.S.A.* **2015**, *112*, E194−E203.
(14) Bowden, J. A.; Heckert, A.; Ulmer, C. Z.; Jones, C. M.; Koelmel, J. P.; Abdullah, L.; Ahonen, L.; Alnouti, Y.; Armando, A.; Asara, J. M.; et al. Harmonizing Lipidomics: NIST Interlaboratory Comparison Exercise for Lipidomics Using Standard Reference Material 1950 Metabolites in Frozen Human Plasma. *J. Lipid Res.* **2017**, *58*, 2275−2288.
(15) Aksenov, A. A.; Silva, R.; da; Knight, R.; Lopes, N. P.; Dorrestein, P. C. Global Chemical Analysis of Biology by Mass Spectrometry. *Nat. Rev. Chem.* **2017**, *1*, 0054.
(16) Fessenden, M. Metabolomics: Small Molecules, Single Cells. *Nature* **2016**, *540*, 540153a.
(17) Yu, Z.; Kastenmüller, G.; He, Y.; Belcredi, P.; Möller, G.; Prehn, C.; Mendes, J.; Wahl, S.; Roemisch-Margl, W.; Ceglarek, U.; et al. Differences between Human Plasma and Serum Metabolite Profiles. *PLOS ONE* **2011**, *6*, No. e21230.
(18) Keleştemur, S.; Çulha, M. Understanding and Discrimination of Biofilms of Clinically Relevant Microorganisms Using Surface-Enhanced Raman Scattering. *Appl. Spectrosc.* **2017**, *71*, 1180−1188.
(19) Žukovskaja, O.; Jahn, I. J.; Weber, K.; Cialla-May, D.; Popp, J. Detection of Pseudomonas Aeruginosa Metabolite Pyocyanin in Water and Saliva by Employing the SERS Technique. *Sensors* **2017**, *17*, 1704.
(20) Bodelón, G.; Montes-García, V.; López-Puente, V.; Hill, E. H.; Hamon, C.; Sanz-Ortiz, M. N.; Rodal-Cedeira, S.; Costas, C.; Celiksoy, S.; Pérez-Juste, I.; et al. Detection and Imaging of Quorum Sensing in Pseudomonas Aeruginosa Biofilm Communities by Surface-Enhanced Resonance Raman Scattering. *Nat. Mater.* **2016**, *15*, 1203−1211.
(21) Nam, J.-M.; Oh, J.-W.; Lee, H.; Suh, Y. D. Plasmonic Nanogap-Enhanced Raman Scattering with Nanoparticles. *Acc. Chem. Res.* **2016**, *49*, 2746−2755.
(22) Lee, J.-H.; Nam, J.-M.; Jeon, K.-S.; Lim, D.-K.; Kim, H.; Kwon, S.; Lee, H.; Suh, Y. D. Tuning and Maximizing the Single-Molecule Surface-Enhanced Raman Scattering from DNA-Tethered Nanodumbbells. *ACS Nano* **2012**, *6*, 9574−9584.
(23) Zhu, W.; Crozier, K. B. Quantum Mechanical Limit to Plasmonic Enhancement as Observed by Surface-Enhanced Raman Scattering. *Nat. Commun.* **2014**, *5*, 5228.
(24) Le Ru, E. C.; Grand, J.; Sow, I.; Somerville, W. R. C.; Etchegoin, P. G.; Treguer-Delapierre, M.; Charron, G.; Félidj, N.; Lévi, G.; Aubard, J. A Scheme for Detecting Every Single Target Molecule with Surface-Enhanced Raman Spectroscopy. *Nano Lett.* **2011**, *11*, 5013−5019.
(25) Le Ru, E. C.; Meyer, M.; Etchegoin, P. G. Proof of Single-Molecule Sensitivity in Surface Enhanced Raman Scattering (SERS) by Means of a Two-Analyte Technique. *J. Phys. Chem. B* **2006**, *110*, 1944−1948.
(26) Zrimsek, A. B.; Wong, N. L.; Van Duyne, R. P. Single Molecule Surface-Enhanced Raman Spectroscopy: A Critical Analysis of the Bianalyte versus Isotopologue Proof. *J. Phys. Chem. C* **2016**, *120*, 5133−5142.
(27) Woehl, T. J.; Heatley, K. L.; Dutcher, C. S.; Talken, N. H.; Ristenpart, W. D. Electrolyte-Dependent Aggregation of Colloidal Particles near Electrodes in Oscillatory Electric Fields. *Langmuir* **2014**, *30*, 4887−4894.
(28) Nadal, F.; Argoul, F.; Hanusse, P.; Pouligny, B.; Ajdari, A. Electrically Induced Interactions between Colloidal Particles in the Vicinity of a Conducting Plane. *Phys. Rev. E: Stat., Nonlinear, Soft Matter Phys.* **2002**, *65*, 061409.
(29) Böhmer. In Situ Observation of 2-Dimensional Clustering during Electrophoretic Deposition. *Langmuir* **1996**, *12*, 5747−5750.
(30) Sides, P. J. Electrohydrodynamic Particle Aggregation on an Electrode Driven by an Alternating Electric Field Normal to It. *Langmuir* **2001**, *17*, 5791−5800.
(31) Thrift, W. J.; Nguyen, C. Q.; Darvishzadeh-Varcheie, M.; Zare, S.; Sharac, N.; Sanderson, R. N.; Dupper, T. J.; Hochbaum, A. I.; Capolino, F.; Qomi, M. J. A.; et al. Driving Chemical Reactions in Plasmonic Nanogaps with Electrohydrodynamic Flow. *ACS Nano* **2017**, *11*, 11317−11329.
(32) Koh, A. L.; Bao, K.; Khan, I.; Smith, W. E.; Kothleitner, G.; Nordlander, P.; Maier, S. A.; McComb, D. W. Electron Energy-Loss Spectroscopy (EELS) of Surface Plasmons in Single Silver Nanoparticles and Dimers: Influence of Beam Damage and Mapping of Dark Modes. *ACS Nano* **2009**, *3*, 3015−3022.
(33) Lyandres, O.; Shah, N. C.; Yonzon, C. R.; Walsh, J. T.; Glucksberg, M. R.; Van Duyne, R. P. Real-Time Glucose Sensing by Surface-Enhanced Raman Spectroscopy in Bovine Plasma Facilitated by a Mixed Decanethiol/Mercaptohexanol Partition Layer. *Anal. Chem.* **2005**, *77*, 6134−6139.
(34) Cheung, W.; Shadi, I. T.; Xu, Y.; Goodacre, R. Quantitative Analysis of the Banned Food Dye Sudan-1 Using Surface Enhanced Raman Scattering with Multivariate Chemometrics. *J. Phys. Chem. C* **2010**, *114*, 7285−7290.
(35) Dong, R.; Weng, S.; Yang, L.; Liu, J. Detection and Direct Readout of Drugs in Human Urine Using Dynamic Surface-Enhanced Raman Spectroscopy and Support Vector Machines. *Anal. Chem.* **2015**, *87*, 2937−2944.
(36) Trau, M.; Saville, D. A.; Aksay, I. A. Assembly of Colloidal Crystals at Electrode Interfaces. *Langmuir* **1997**, *13*, 6375−6381.
(37) Squires, T. M.; Bazant, M. Z. Induced-Charge Electro-Osmosis. *J. Fluid Mech.* **2004**, *509*, 217−252.
(38) Watson, D.; MacDermot, J.; Wilson, R.; Cole, P. J.; Taylor, G. W. Purification and Structural Analysis of Pyocyanin and 1-Hydroxyphenazine. *Eur. J. Biochem.* **1986**, *159*, 309−313.
(39) Wu, X.; Chen, J.; Li, X.; Zhao, Y.; Zughaier, S. M. Culture-Free Diagnostics of Pseudomonas Aeruginosa Infection by Silver Nanorod Array Based SERS from Clinical Sputum Samples. *Nanomed. Nanotechnol. Biol. Med.* **2014**, *10*, 1863−1870.
(40) Armbruster, D. A.; Pry, T. Limit of Blank, Limit of Detection and Limit of Quantitation. *Clin. Biochem. Rev.* **2008**, *29*, S49−S52.
(41) Qi, G.; Jia, K.; Fu, C.; Xu, S.; Xu, W. A Highly Sensitive SERS Sensor for Quantitative Analysis of Glucose Based on the Chemical Etching of Silver Nanoparticles. *J. Opt.* **2015**, *17*, 114020.
(42) Grubisha, D. S.; Lipert, R. J.; Park, H.-Y.; Driskell, J.; Porter, M. D. Femtomolar Detection of Prostate-Specific Antigen: An Immunoassay Based on Surface-Enhanced Raman Scattering and Immunogold Labels. *Anal. Chem.* **2003**, *75*, 5936−5943.
(43) Srichan, C.; Ekpanyapong, M.; Horprathum, M.; Eiamchai, P.; Nuntawong, N.; Phokharatkul, D.; Danvirutai, P.; Bohez, E.; Wisitsoraat, A.; Tuantranont, A. Highly-Sensitive Surface-Enhanced Raman Spectroscopy (SERS)-Based Chemical Sensor Using 3D Graphene Foam Decorated with Silver Nanoparticles as SERS Substrate. *Sci. Rep.* **2016**, *6*, 23733.
(44) Lee, D.; Lee, S.; Seong, G. H.; Choo, J.; Lee, E. K.; Gweon, D.-G.; Lee, S. Quantitative Analysis of Methyl Parathion Pesticides in a Polydimethylsiloxane Microfluidic Channel Using Confocal Surface-Enhanced Raman Spectroscopy. *Appl. Spectrosc.* **2006**, *60*, 373−377.
(45) Stevenson, R.; Ingram, A.; Leung, H.; McMillan, D. C.; Graham, D. Quantitative SERRS Immunoassay for the Detection of Human PSA. *Analyst* **2009**, *134*, 842−844.
(46) Theis, K. R.; Venkataraman, A.; Dycus, J. A.; Koonter, K. D.; Schmitt-Matzen, E. N.; Wagner, A. P.; Holekamp, K. E.; Schmidt, T. M. Symbiotic Bacteria Appear to Mediate Hyena Social Odors. *Proc. Natl. Acad. Sci. U.S.A.* **2013**, *110*, 19832−19837.
(47) Nguyen, C.; Thrift, W.; Bhattacharjee, A.; Whiteson, K.; Hochbaum, A.; Ragan, R. Robust SERS Spectral Analysis for

DOI: 10.1021/acsami.7b18592
ACS Appl. Mater. Interfaces XXXX, XXX, XXX−XXX

Quantitative Detection of Pycocyanin in Biological Fluids. *Biosensing and Nanomedicine X, Proceedings of SPIE Nanoscience + Engineering*; International Society for Optics and Photonics: San Diego, CA, Aug 6−10, 2017.
(48) Reszka, K. J.; O'Malley, Y.; McCormick, M. L.; Denning, G. M.; Britigan, B. E. Oxidation of Pyocyanin, a Cytotoxic Product from Pseudomonas Aeruginosa, by Microperoxidase 11 and Hydrogen Peroxide. *Free Radical Biol. Med.* **2004**, *36*, 1448−1459.
(49) Dietrich, L. E. P.; Price-Whelan, A.; Petersen, A.; Whiteley, M.; Newman, D. K. The Phenazine Pyocyanin Is a Terminal Signalling Factor in the Quorum Sensing Network of Pseudomonas Aeruginosa. *Mol. Microbiol.* **2006**, *61*, 1308−1321.
(50) Bhattacharjee, A.; Khan, M.; Kleiman, M.; Hochbaum, A. I. Effects of Growth Surface Topography on Bacterial Signaling in Coculture Biofilms. *ACS Appl. Mater. Interfaces* **2017**, *9*, 18531−18539.
(51) Adams, S. M.; Campione, S.; Caldwell, J. D.; Bezares, F. J.; Culbertson, J. C.; Capolino, F.; Ragan, R. Non-Lithographic SERS Substrates: Tailoring Surface Chemistry for Au Nanoparticle Cluster Assembly. *Small* **2012**, *8*, 2239−2249.
(52) Rahme, L. G.; Stevens, E. J.; Wolfort, S. F.; Shao, J.; Tompkins, R. G.; Ausubel, F. M. Common Virulence Factors for Bacterial Pathogenicity in Plants and Animals. *Science* **1995**, *268*, 1899−1902.
(53) Monahan, L. G.; Turnbull, L.; Osvath, S. R.; Birch, D.; Charles, I. G.; Whitchurch, C. B. Rapid Conversion of Pseudomonas Aeruginosa to a Spherical Cell Morphotype Facilitates Tolerance to Carbapenems and Penicillins but Increases Susceptibility to Antimicrobial Peptides. *Antimicrob. Agents Chemother.* **2014**, *58*, 1956−1962.
(54) Parker, J. H.; Feldman, D. W.; Ashkin, M. Raman Scattering by Silicon and Germanium. *Phys. Rev.* **1967**, *155*, 712−714.
(55) Geladi, P.; Kowalski, B. R. Partial Least-Squares Regression: A Tutorial. *Anal. Chim. Acta* **1986**, *185*, 1−17.
(56) Adams, S. M.; Campione, S.; Capolino, F.; Ragan, R. Directing Cluster Formation of Au Nanoparticles from Colloidal Solution. *Langmuir* **2013**, *29*, 4242−4251.
(57) Grady, N. K.; Halas, N. J.; Nordlander, P. Influence of Dielectric Function Properties on the Optical Response of Plasmon Resonant Metallic Nanoparticles. *Chem. Phys. Lett.* **2004**, *399*, 167−171.
(58) Moerland, R. J.; Hoogenboom, J. P. Subnanometer-Accuracy Optical Distance Ruler Based on Fluorescence Quenching by Transparent Conductors. *Optica* **2016**, *3*, 112−117.

DOI: 10.1021/acsami.7b18592
ACS Appl. Mater. Interfaces XXXX, XXX, XXX−XXX